Journal of Materials Science: Materials in Electronics (2020) 31:8618–8626
https://doi.org/10.1007/s10854-020-03397-5

Superior photoanode based on nanostructured TiO_2@reduced graphene oxide composite with enhanced photo-to-electron conversion efficiency

Junxiong Guo[1] · **Shangdong Li**[1] · **Yizhen Ke**[1] · **Yiyi Li**[1] · **Xumei Cui**[2] · **Hua Chen**[3] · **Yu Liu**[4] · **Linna Mao**[1] · **Wen Huang**[1]

Received: 16 November 2019 / Accepted: 10 April 2020 / Published online: 20 April 2020

Abstract

Conformal structured TiO_2-reduced graphene oxide composite nanosheets (TiO_2@rGO CNS) have been synthesized by a one-step hydrothermal method. The prepared TiO_2 composite features a two-dimensional (2D) structure with an ultra-large specific surface area of 269 $m^2 g^{-1}$ and homogeneous TiO_2 nanoparticles directly grown on the surface of reduced graphene oxide (rGO) sheets. With this special architecture of 2D sheet, it gives rise to improve light-harvesting and photo-to-electron conversion efficiency. When the TiO_2@rGO CNS incorporated into the photoanode, it exhibits a greatly enhanced absorption in the visible range and low charge transfer resistance of 10.16 Ω compared with that of bare TiO_2-based electrode (15.22 Ω). When the rGO content in TiO_2@rGO CNS is 0.8 wt%, the fabricated solar cell obtains a remarkably enhanced power conversion efficiency (up to 7.05%), compared with that of the bare TiO_2-based solar cell (4.36%), where the short-circuit current density, open-circuit voltage, and fill factor of the device are 13.63 mA cm^{-2}, 0.712 V, and 0.69, respectively. With the above-mentioned merits, this work supplies a feasible approach for the functionalization of 2D materials decorated with controlled metal oxide nanoparticles, which is expected as a promising material in high-performance photovoltaic devices for practical applications.

1 Introduction

Photoanodes have been considered as a critical component for the photoelectron devices due to its crucial role in light harvest and charge transfer promotion. Among the photoanode materials, TiO_2 has attracted enormous attention due to its merits of strong charge separation capacity, low costs, poor environmental damage, ultra-high chemical/optical stability, and easy preparation [1–5]. Unfortunately, TiO_2 can solely absorb the ultraviolet (UV) light and the inherent low conductivity causes poor charge transport efficiency of the photon-generated electron limited by the wide bandgap of 3.2 eV, leading to a low photo-to-electron conversion efficiency [6, 7]. To solve these problems, the combination of semiconductors with high specific surface area and conductive materials, such as carbon nanotube (CNT) or graphene, has been investigated to improve the visible light-harvesting efficiency and enhance the electronic conductivity for charge transfer, thus improving the photoelectric performance of related photoanodes [8, 9]. However, the nanoparticles loaded on the surface of CNT or graphene still suffer from the chemical inertness induced by the lack of reactive oxygen moieties, leading to the difficulty of functionalization in the synthesis process [10, 11].

Electronic supplementary material The online version of this article (https://doi.org/10.1007/s10854-020-03397-5) contains supplementary material, which is available to authorized users.

✉ Xumei Cui
cuixumei@163.com

✉ Yu Liu
y-liu-17@mails.tsinghua.edu.cn

✉ Wen Huang
uestchw@uestc.edu.cn

[1] State Key Laboratory of Electronic Thin Films and Integrated Devices, School of Electronic Science and Engineering (National Exemplary School of Microelectronics), University of Electronic Science and Technology of China, Chengdu 610054, China

[2] College of Optoelectronic Engineering, Chengdu University of Information Technology, Chengdu 610225, China

[3] School of Vanadium and Titanium, Panzhihua University, Panzhihua 617000, China

[4] Institute of Microelectronics and Tsinghua National Laboratory for Information Science and Technology (TNList), Tsinghua University, Beijing 100084, China

Recently, using semiconductor/reduced graphene oxide (rGO) nanocomposites as different materials applications, e.g., enhanced photocatalytic activity [12–14] and improved photovoltaic performance [15, 16], has attracted many research interests. In particular, a method to combine rGO with mesoporous TiO_2 provides a promising method for high photoelectric performance of anode [17–19]. When the ultra-large surface area of rGO sheets serves as the support substrates for coating TiO_2 nanoparticles, it offers a new pathway for charge transport due to the high conductivity of $-99\ S\ cm^{-1}$ [20–22]. Zhao et al.[23] used TiO_2 nanorods loaded on rGO as photoanode, and the fabricated solar cell achieved a higher power conversion efficiency, which is increased by 17.7% compared with that of bare TiO_2. Liu et al.[24] found that the incident photon-to-current conversion efficiency gradually increases with rGO content from 0.0 to 0.75 wt% and then decreases at rGO over 0.75 wt% loading in their TiO_2 composites. These researches effectively improved the photocurrent but the fill factor (*FF*) was still low, even worse than that of bare TiO_2 [25]. On the other hand, the most reported TiO_2-rGO composite, at present, is a disordered and random distribution of rGO, leading to a low charge transfer efficiency due to the high recombination possibility of the photogenerated carrier in the transport routes [19, 26–28]. Therefore, it is highly desirable to develop a facile method for preparing conformal nanostructured TiO_2-rGO composite, in which rGO sheet with controlled weight content coated by TiO_2 nanoparticles and forming a well-ordered mesoporous film.

Herein, we report a two-dimensional structured TiO_2-covered rGO composite nanosheets (TiO_2@rGO CNS) prepared by covering the titania precursor on the surface of graphene oxide (GO) with the one-step hydrothermal process, and then direct fabrication mesoporous anode by a doctor-blade method. The achieved TiO_2@rGO CNS not only possesses uniform distributed anatase TiO_2, controllable rGO content from 0–1.2 wt%, and ultra-high specific surface area, but also exhibits a low charge transfer resistance and long electron lifetime at the interfaces of the fabricated anode. In addition, the fabricated photoanodes based on TiO_2@rGO CNS are applied in the solar cell devices and achieve a dramatically enhanced power conversion efficiency of 7.05% with *FF* of 0.69, compared with that of bare TiO_2 of 4.36% with *FF* of 0.61.

2 Experimental section

2.1 Synthesis of materials

Figure 1a illustrates the typical route for TiO_2 and related TiO_2@rGO composite synthesis using the hydrothermal method. All chemicals were analytical grade reagents and used without further purification. Graphene oxide (GO) dispersion (1 mg/mL) was obtained with the improved Hummers method [29]. Titanium isopropoxide (TTIP) (3.56 mL) was added to glacial acetic acid (15 mL). The obtained solution was then added dropwise in a mixture of synthesized GO dispersion (0–12 mL), deionized (DI) water (12–0 mL) and ethanol absolute to form a homogeneous solution after magnetic stirring for several hours at ice-bath. The total volume of the solution was 80 mL. The formed titania precursor was then transferred into a p-polyphenylene-lined autoclave (100 mL) and kept at 180 ℃ for 12 h. The oxygen-containing groups in GO (left column of Fig. 1a) facilitate metal oxides (e.g., TiO_2) to easily cover the GO sheets and disperse in oxygen-containing solvent (e.g., H_2O, CH_3CH_2OH) [30]. Interestingly, the GO sheets are synchronously reduced in the crystallized process of titanium precursor during the thermal process [27, 31]. Then, the gray or white precipitates were washed alternately with ethanol and deionized water several times via centrifugation after annealing. The bare TiO_2 was obtained in the same way without added GO dispersion. Finally, the as-prepared bare TiO_2 (0 mL GO dispersion) and TiO_2@rGO CNS (2–12 mL GO dispersion) were dried at 90 ℃ for 2 h at vacuum oven.

2.2 Fabrication of device

Figure 1b shows the fabrication process for the as-prepared materials-based mesoporous films using the doctor-blade method [32]. Briefly, we prepared a homogeneous paste, which consists of bare TiO_2 (or TiO_2 composites), polyethylene glycol (PEG-2000), DI water, and ethanol by the mass ratio of 2:1:10:20, using a balling technique. Then, we transferred the paste onto a clean FTO glass with a mask, and then formed a ribbon of $5 \times 20\ mm^2$. The thickness of the obtained film was around 12 μm examined by a step profiler. Finally, we placed the naturally leveling paste on FTO glass in an oven to remove the exceeded organic materials and form mesoporous film via annealing. The optical images of the fabricated mesoporous films are shown in the top column of Fig. 1b. Obviously, the bare TiO_2 and of TiO_2-rGO composite-based film can be initially recognized by the color, which exhibits white and gray colors, respectively.

Subsequently, the obtained mesoporous films were immersed into 0.5 mM N719 ruthenium complex dye solution with absolute ethanol for overnight at room temperature in the dark. The dye-sensitized film was rinsed with ethanol to remove residual dye molecules and dried. The sensitized photoanode and the Pt-covered counter electrode were encapsulated using a heat-sealing film and the electrolyte was injected through a hole with a diameter of 0.5 mm on the counter electrode edge. The electrolyte solution was 0.6 M DMPII, 0.1 M LiI, 0.03 M I_2, and 0.5 M TBP in

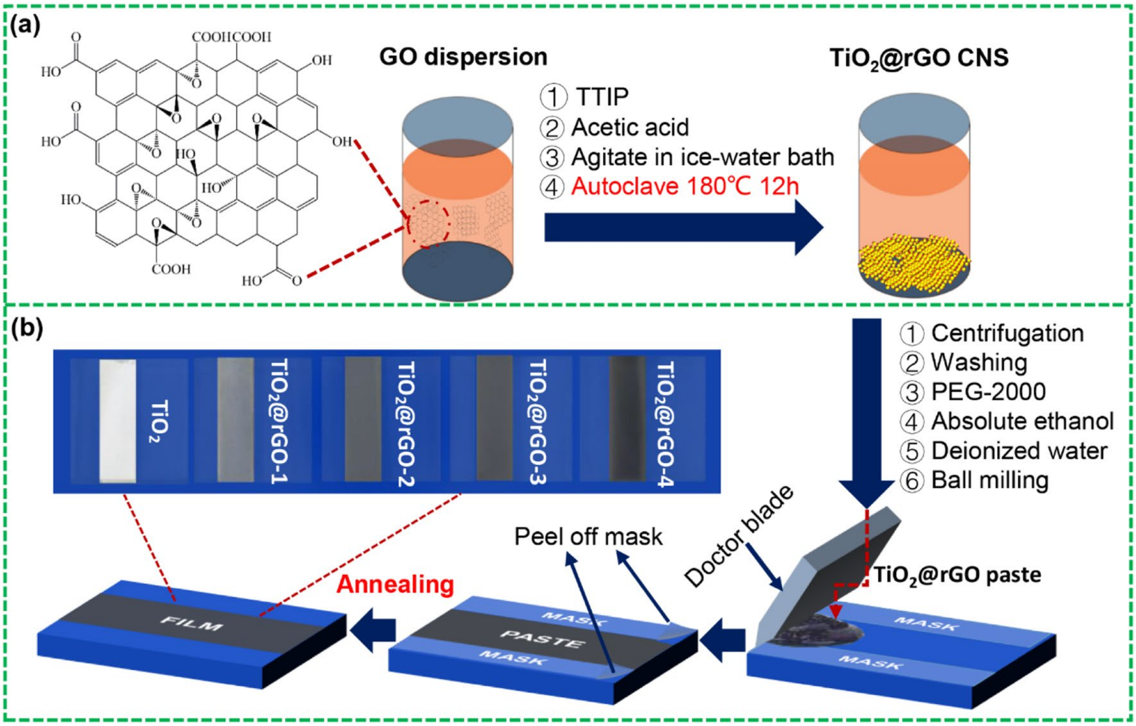

Fig. 1 Scheme of preparation of TiO_2@rGO CNS and related anodes. **a** Synthesis process of TiO_2@rGO CNS. The inset (left) is the suggested molecular model of GO. **b** Fabrication process of photoanode based on TiO_2@rGO CNS. The inset (top) is optical images of TiO2@rGO CNS-based anodes with controllable rGO content. TiO_2, TiO_2@rGO-1, TiO_2@rGO-2, TiO_2@rGO-3, and TiO_2@rGO-4 indicate 0, 0.2, 0.5, 0.8, and 1.2 wt% rGO in TiO_2@rGO CNS, respectively

acetonitrile. The hole was also sealed using a heat-sealing film. The active area of our devices was 5×5 mm^2.

2.3 Measurements and characterization

The morphology and structure of samples were characterized by a field emission scanning electron microscopy (FE-SEM, JEOL JSM-7500F) and atomic force microscopy (AFM, Bruker Dimension D3100). The thickness of the prepared film was examined using a step profiler (Bruker DektakXT). The crystalline structure was obtained by employing X-ray diffraction (XRD, SHIMADZU XRD-7000) with a Cu Kα radiation ($\lambda = 1.5418$ Å) and Raman shift with 532 nm laser wavelength at room temperature in the spectral range of 75−3200 cm^{-1}, as well as X-ray photoelectron spectroscopy (XPS, Kratos XSAM800). Brunauer–Emmett–Teller (BET) method and nitrogen adsorption/desorption measurement at 77 K (Gemini V ASAP-2010) were employed to characterize the pore structures. The ultraviolet–visible (UV–Vis) spectra were measured by a spectrophotometer (Agilent Cary5000). The monochromatic incident photon-to-electron conversion efficiency (IPCE) was measured with a quantum efficiency system (PV Measurements QEX10-PP). Photovoltaic characters of the dye-sensitized solar cell (DSSC) including current density/voltage (*J*-*V*) and electrochemical impedance spectrum (EIS) at 0.1–10^5 Hz employed a solar simulator (BOS-500X-Z, Changchun, China) at 960 W/m^2 associated with an electrochemical workstation (CHI660C, Shanghai, China).

3 Results and discussion

The morphology of the as-prepared TiO_2@rGO CNS samples was examined by scanning electron microscopy (SEM) and atomic force microscopy (AFM). As shown in Fig. 2a, the synthesized TiO_2 composite is a two-dimensional shape with the lateral size of micrometer order and thickness of nanometer order. Figure 2b shows the SEM image of the rough surface of bare TiO_2 nanoparticles synthesized using the same method. Obviously, the distribution of TiO_2 nanoparticles in composites is similar to that of bare TiO_2. The controllable rGO content in prepared composite materials is proved by the AFM. Figure 2c, d shows the average height of TiO_2@rGO CNS with 0.2 wt% and 1.2 wt% rGO, respectively. Evidently, the content of TiO_2 coating on the surface of rGO sheet is easily tuned by controlling the introduction of rGO content. Figure 2e, f shows the energy distribution spectroscopy (EDS) of synthesized materials. According to the element distribution intensity, the carbon contents of

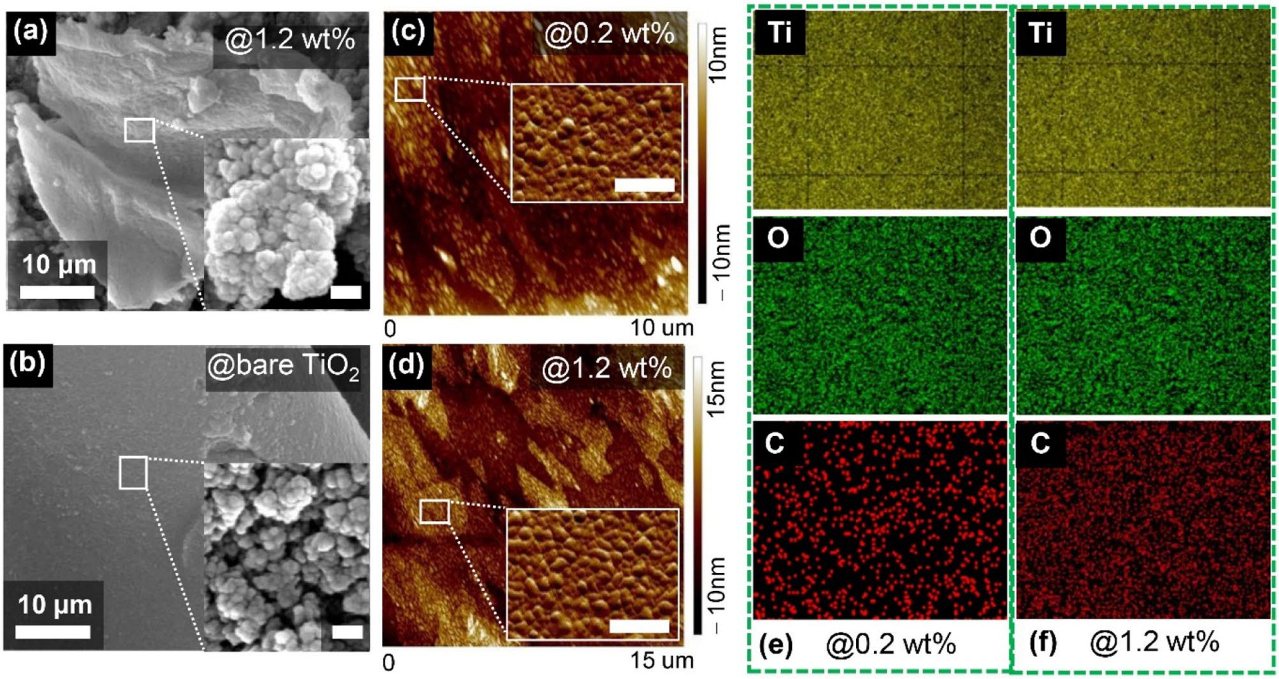

Fig. 2 Morphology of synthesized bare TiO_2 and TiO_2@rGO CNS. SEM images of prepared **a** TiO_2@rGO CNS and **b** bare TiO_2. The insets are the high-resolution SEM images of synthesized TiO_2 nanoparticles. AFM image of **c** 0.2 wt% and **d** 1.2 wt% rGO in TiO_2@rGO CNS. The insets are the high-resolution AFM images corresponding to the TiO_2 nanoparticles grown on the rGO sheets. EDS images for Ti, O, and C elements mapping of **e** 0.2 wt% and **f** 1.2 wt% rGO in TiO_2@rGO CNS

0.2 wt% and 1.2 wt% rGO in prepared composites are quite different, which further confirms the rGO of the composite can be easily controlled by the addition of GO dispersion. Meanwhile, the AFM images (insets of Fig. 2c, d) show a consistent result with SEM images (insets of Fig. 2a, b), namely the shape of the composite is nanosheet composed by rGO sheet covered with a nanoscale size of TiO_2.

As shown in Fig. 3a, the X-ray diffraction (XRD) pattern of the bare TiO_2 and TiO_2@rGO CNS exhibits well-defined diffraction peaks, which can be well indexed to the typical anatase phase (ICSD No. 009855). The diffraction peak of − 23.76° can be contacted with the phase of (0 0 2) of reduced graphene oxide [33]. Of particular note that the peak at around 23.76° occurs evidently in the TiO_2@rGO when the content of rGO in composite exceeds 5.0 wt%, as shown in Fig. S1 (*Supplementary Information*). This trend may be connected with the nature of regular stack of rGO destroyed by the intercalation of TiO_2 when the content of rGO is less than 5.0 wt% [34, 35]. The average crystal size of the TiO_2 nanoparticles is calculated to be about 20 nm from the (1 0 1) plane diffraction peak at around 25.3° by the Scherrer equation [2], which is consistent with the above-mentioned morphology images (Fig. 2a–d). As shown in Fig. 3b, the Raman spectra of bare TiO_2 and TiO_2@rGO CNS display signal at 142 cm^{-1}, 478 cm^{-1}, 519 cm^{-1}, and 635 cm^{-1}, which are contacted as E_g band, E_{1g} band, $E_{1g}E_{2g}$ band, and E_g band of anatase phase TiO_2, respectively [36]. The other two signals at 1343 cm^{-1} and 1602 cm^{-1} are corresponding to the D band and G band of rGO, respectively [37]. The shift of the G band compared to that of bare rGO may connect with the interaction between the rGO sheets and the surface TiO_2 nanoparticles [38–40].

XPS spectroscopy was employed to confirm the rGO sheets in TiO_2@rGO CNS, reduced from GO in titanium precursor by hydrothermal method, shown in Fig. S2 (*Supplementary Information*). Figure 3c–e documents the XPS peaks of the as-prepared TiO_2@rGO CNS. As depicted in Fig. 3c, the energy binding peak of C 1 s at 284.5 eV, 285.6 eV, and 288.3 eV attach to the C–C/C= bond, C–O, and C=O/O–C= O bond, respectively [41, 42]. The Ti 2p peaks at 459.3 eV of Ti $2p_{3/2}$, 462.4 eV of Ti $2p_{1/2}$ (Fig. 3d), and Ti–O bonds (Fig. 3e) are slightly shifted than that of bare TiO_2 [43]. This shift is resulted by a strong electron interaction between the rGO sheets and TiO_2 particles as well as the partial formation of Ti–O–C bonds, which is consistent with the Raman shift in Fig. 3b. A similar result is also observed in other TiO_2-based composite, such as TiO_2@C core–shell structured nanomaterials [44].

The specific surface area and pore size distribution of the prepared bare TiO_2 nanoparticles and TiO_2@rGO CNS were investigated by nitrogen adsorption/desorption measurement with the Brunauer–Emmett–Teller (BET) method.

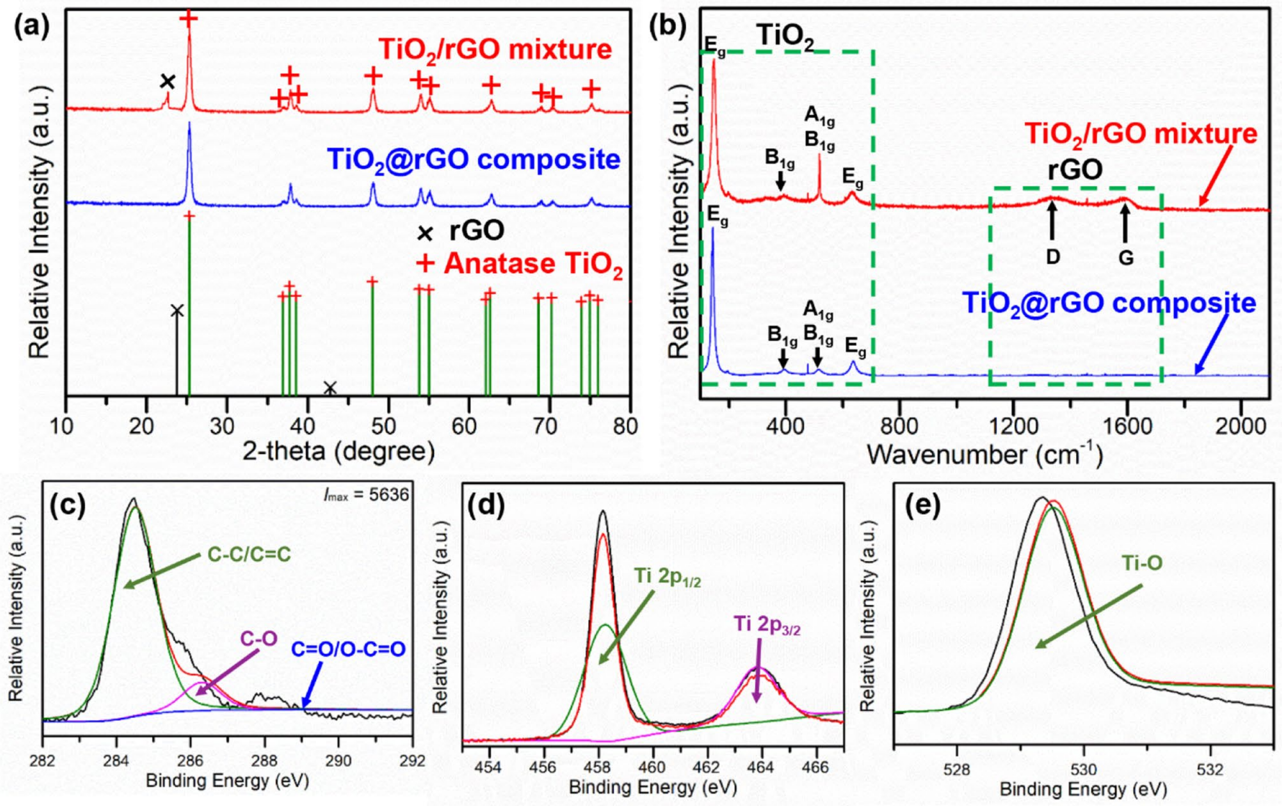

Fig. 3 Characterization for the structure of synthesized TiO_2@rGO CNS. **a** XRD spectrum of TiO_2@rGO CNS and bare TiO_2. The TiO_2/rGO mixture is fomed using ultrasonication to disperse the bare TiO_2 in the rGO solution. The rGO content in synthezed TiO_2@rGO composite is 1.2 wt%. **b** Raman spectroscopy of TiO_2@rGO CNS and bare TiO_2. **c** C1s, **d** Ti 2p, and **e** Ti-O bond spectra of XPS for TiO_2@rGO CNS

The results of N_2 adsorption/desorption isotherms with an H_2 hysteresis loop are shown in Fig. 4a. It shows that the specific surface area of bare TiO_2 and TiO_2@rGO CNS with 0.8 wt% rGO is – 152 m^2/g and – 269 m^2/g, respectively, indicating that the introduction of reduced graphene oxide sheets exerts a strong positive effect on morphology structure. Benefited from the ultra-large specific surface area, the TiO_2@rGO CNS potentially provides more active sites for sensitizer adsorption to produce photo-induced carriers compared with the bare TiO_2 [45]. The pore size distribution of the fabricated electrodes is shown in Fig. 4b. Compared with bare TiO_2 whose pore size concentrating near – 1 nm and – 4 nm, the TiO_2@rGO CNS with 0.8 wt% rGO possesses an even pore size distribution centralized within around 5 nm, which is convenient for the diffusion of redox couple [32, 45].

Fig. 4 **a** Nitrogen adsorption/desorption isotherms and **b** pore size distribution of bare TiO_2 and TiO_2@rGO CNS

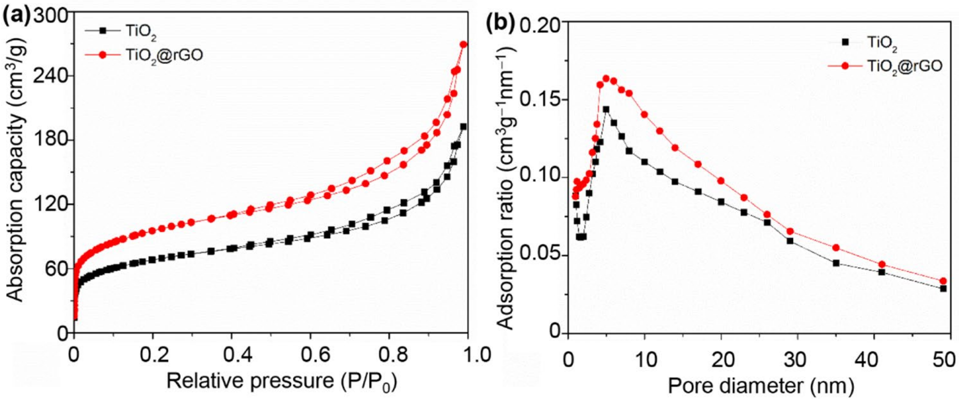

To explore the performance of photo-to-electron conversion, we used the prepared bare TiO_2 and TiO_2@rGO CNS (0.2 −1.2 wt% rGO) as active materials to fabricate photoanodes (Fig. 1b). Firstly, we employed an ultraviolet–visible (UV–Vis) spectroscopy to justify the light-harvesting capability of the prepared photoanodes. Figure 5a shows that all the photoanodes based on TiO_2@rGO CNS possess enhanced absorption in the visible region, especially at the wavelengths of around 350 nm and 530 nm, compared with the bare TiO_2-based photoanode. Meanwhile, the monochromatic incident photon-to-electron conversion efficiency (IPCE) spectroscopy was used to investigate the light-harvesting capacity of according electrodes with different contents of rGO, shown in Fig. 5b. The intensity of IPCE increases with the increasing incorporation of rGO from 0.2 wt% to 0.8 wt%. The enhanced IPCE may be attributed to the significant improvement of specific surfaces in the prepared composites, who can adsorb more sensitizer to generate photo-induced carriers compared with the bare TiO_2 [45]. However, the TiO_2@rGO-4 (1.2 wt% rGO)-based photoanode exhibits a poor IPCE performance, although the corresponding photoanode possesses the highest photon absorption intensity. The fall of IPCE in photoanode could be associated with the exceeded rGO (1.2 wt%) in TiO_2@rGO CNS that generates superfluous trapping sites to enhance the photon absorption; however, it also produces excessive recombination sites to increase dark current [46].

To further investigate the behavior of the photo-induced carrier in prepared photoanodes, the electrochemical impedance spectrum (EIS) was applied to explore the characteristics of the recombination and transport of the carrier at the interfaces. A typical Nyquist plot consists of three semicircles along with the increasing frequency, which is corresponding to the Nernst diffusion in the electrolyte (R_s), the charge transfer resistance at the photoanode with dye/electrolyte interface (R_2) and the counter electrode/electrolyte interface (R_1), respectively [47]. In general, R_2 is the distinct difference which is determined by the diameter of the corresponding semicircle, while R_s and R_1 are seemly identical due to the consistency of employing the same electrolyte and counter electrode. Obviously, the R_2 value in the dark condition of Fig. 5c grows as the introduction of rGO increases in photoanodes, which indicates that TiO_2@rGO electrodes can efficiently prevent the recombination of the photogenerated carrier. Meanwhile, according to the EIS plots at illumination shown in Fig. 5d, the R_2 of TiO_2@rGO-0.8 wt% possesses the minimum value (10.16 Ω), rather than TiO_2@rGO-1.2 wt% (19.02 Ω) which is even higher than that of bare TiO_2 (15.22 Ω). These indicate that the appropriate addition of rGO can enhance the transportation of carrier, while an excessive introduction of it will exert a negative impact. Besides, the photogenerated electron lifetime (τ_e) during the cell operation can be calculated with the formula $\tau_e = 1/(2\pi \times f_{max})$ from the Bode plots [47, 48]. Here f_{max} is

Fig. 5 Photoresponse of bare TiO_2 and TiO_2@rGO CNS-based electrodes. **a** UV–Vis absorption spectroscopy. **b** IPCE curves. **c** EIS curves in dark. **d** EIS curves under illumination with incident power of 960 W/cm^2

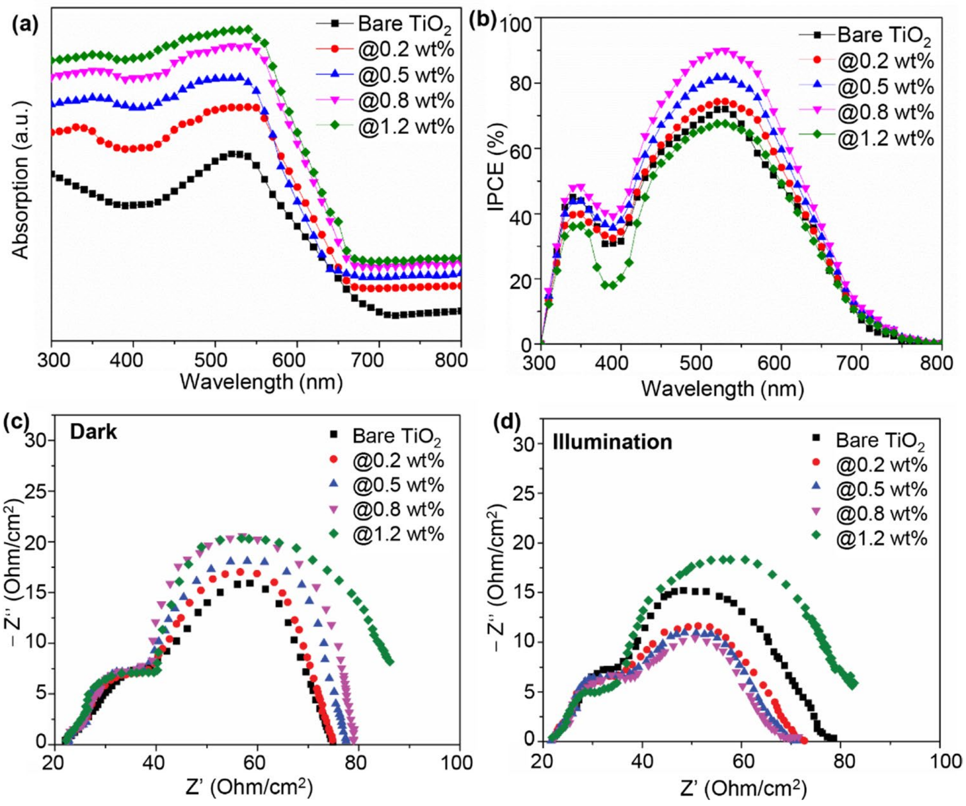

the frequency at the maximum phase angle (Fig. S3, Supplementary Information). The f_{max} of TiO_2@rGO-0.8 wt% (19 Hz) is much lower than that of the bare TiO_2 (146 Hz), indicating a much longer electron lifetime in TiO_2@rGO-0.8 wt% (8.28 ms) than in bare TiO_2 (1.09 ms). It indicates that a smaller charge recombination probability and subsequently improves the photon-to-electron transport efficiency of the fabricated photoanodes, which is consistent with the results of IPCE (Fig. 5b).

Benefited from the ultra-high performance of photo-to-electron conversion, the prepared TiO_2@rGO could be one of the best candidates of next-generation photoelectric devices, such as solar cell, photocatalysis, and others. Herein, we used the electrodes based on TiO_2@rGO as anodes for the application of DSSC. The photovoltaic performances of the fabricated DSSC based on TiO_2@rGO CNS are shown in Fig. 6a. It can be observed that the open-circuit voltage (V_{OC}) of assembled DSSC is around 0.71 V, which is dominantly determined by the potential difference between the Fermi level of the illuminated mesoporous TiO_2 semiconductor and the Nernst potential of I^-/I_3^- redox couple in the liquid electrolyte. The short-circuit current density (J_{SC}) reaches to 10.40, 12.05, and 13.63 mA/cm^2 for different photoanodes fabricated with 0.2, 0.5, and 0.8 wt% rGO in TiO_2@rGO CNS, respectively. The reasons for this significantly improved Jsc could be explained as follows: (1) the ultra-high specific surface of TiO_2@rGO CNS possesses much more positive sites for absorbing sensitizer to generate carriers [40, 49]; (2) the unique structure of the as-prepared TiO_2@rGO CNS induces a low resistance at the interfaces of rGO/TiO_2/dye/electrolyte in DSSC [8, 50]. However, when the excessive content of 1.2 wt% rGO/TiO_2 introduced into the composite nanosheet, the J_{SC} slashes to 8.48 mA/cm^2, even lower than the bare TiO_2 (8.73 mA/cm^2).

All of the photovoltaic performances of DSSC in this work are summarized in Table 1. Obviously, the TiO_2@rGO-3 (0.8 wt% rGO) exhibits a maximum PCE of 7.05%, which is apparently increased in contrast with that of bare TiO_2 of 4.36%. As shown in Table 2, the obtained performances of our device are superior to other TiO_2 composites [3, 4], and are also comparable to the reported TiO_2-rGO composites [25, 40]. Meanwhile, the dark currents in DSSC were investigated, as shown in Fig. 6b. Compared with bare TiO_2, the low dark current density of TiO_2@rGO CNS-based DSSC could be contributed to the photon-induced-current loss derived from the recombination of I_3^- ions in electrolyte [51, 52]. Corresponding with the results of EIS measurement, the calculated J–V curves show that the TiO_2@rGO-4 (1.2 wt% rGO) cell exhibits a higher dark current density at the same potential compared with TiO_2@rGO-3, even higher than bare TiO_2. This trend could be connected with the increasing recombination of photogenerated carriers induced by the exceeded introduction of rGO sheets, which further verify the low IPCE of the fabricated photoanodes (Fig. 5b). Such ultra-high photo-to-electron transport efficiency is also observed in other two-dimensional combined with metal oxide composites, such as g-C_3N_4 co-modified with MnO_x [53], MoS_2 nanofibers combined with TiO_2 [54], graphene nanosheets covered with ZnO [54, 55].

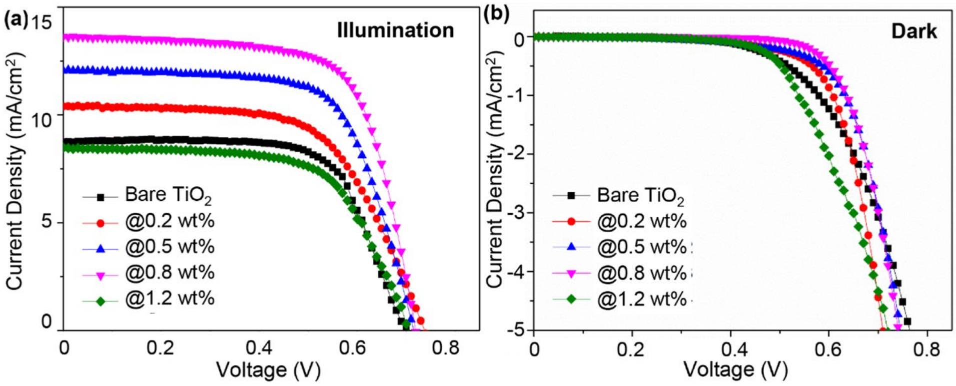

Fig. 6 J–V curves of bare TiO_2 and TiO_2@rGO CNS-based DSSC. **a** Photocurrent of devices under illumination with incident power of 960 W/cm^2. **b** Dark current

Table 1 Photovoltaic parameters of the fabricated DSSC

Sample	J_{SC} (mA/cm^2)	V_{OC} (V)	PCE (%)	FF	rGO (wt%)
Bare TiO_2	8.73 ± 0.05	0.711 ± 0.001	4.36 ± 0.02	0.61 ± 0.08	0
TiO_2@rGO-1	10.40 ± 0.02	0.718 ± 0.003	4.92 ± 0.03	0.63 ± 0.03	0.2
TiO_2@rGO-2	12.05 ± 0.03	0.713 ± 0.002	6.04 ± 0.05	0.67 ± 0.03	0.5
TiO_2@rGO-3	13.63 ± 0.02	0.712 ± 0.002	7.05 ± 0.02	0.69 ± 0.04	0.8
TiO_2@rGO-4	8.48 ± 0.02	0.710 ± 0.003	4.02 ± 0.03	0.65 ± 0.02	1.2

Table 2 Performance comparison of assembled DSSC between our work and other typical TiO_2-based solar cells

Photoanode materials	J_{SC} (mA/cm^2)	V_{OC} (V)	PCE (%)	*FF*	Ref.
TiO_2@rGO-0.8 wt%	13.63 ± 0.02	0.712 ± 0.002	7.05 ± 0.02	0.69 ± 0.04	This work
TiO_2@g-C_3N_4-1.0 wt%	7.43 ± 0.04	0.721 ± 0.002	4.73 ± 0.02	0.53 ± 0.01	[4]
N,S-doped TiO_2	9.78	0.69	3.35	0.50	[3]
TiO_2@rGO composite	16.75	0.74	7.57	0.65	[25]
TiO_2@rGO composite	18.39	0.682	7.68	0.61	[40]

4 Conclusion

In conclusion, the unique structured TiO_2@rGO CNS materials were successfully synthesized by a facile hydrothermal method. Morphology characterization indicates the TiO_2 nanoparticles loading in TiO_2@rGO CNS can be easily tuned by changing the addition of graphene oxide dispersion. The TiO_2@rGO CNS possesses an ultra-large specific surface area up to -269 m^2/g leading to improve photons harvesting and photogenerated carrier generation/separation efficiency in photoanodes. Under the illumination, TiO_2@rGO CNS-based photoanodes own a strong absorption intensity within the wavelength range of UV–Vis, especially at the wavelengths of around 350 nm and 530 nm. Further, the rGO sheets with high conductivity introduced to the mesoporous active layer, rendering the TiO_2@rGO CNS photoanodes own low resistance at the photoanode with dye/electrolyte interface (10.16 Ω) and long electron lifetime (8.28 ms). Benefited from these merits, the solar cell based on TiO_2@rGO composite with 0.8 wt% rGO exhibits both an enhanced fill factor as high as 0.69 and a power conversion efficiency of 7.05%, which is enhanced by 61.7% compared with that of bare TiO_2 of 4.36%. The dual-functional properties of TiO_2@rGO CNS indicate that the two-dimensional reduced graphene oxide can be employed in casting the emerging devices with high performance for photon-to-electron conversion, e.g., solar cells, photocatalysis, and photodegradation.

Acknowledgements The authors acknowledge the financial supports of this work by the National Natural Science Foundation of China (61804023, 61971108), the Open Fund of the State Key Laboratory of Luminescent Materials and Devices (2018-skllmd-06), the Science and Technology Innovation Research Team Construction Project of Sichuan Province (2015TD00008), and the Key R&D Program of Sichuan Province (2017JY0038, 2018GZ0527). We sincerely thank prof. B. Yu for discussion and revision.

Compliance with ethical standards

Conflict of Interest There are no conflicts of interest to declare.

References

1. M. Gratzel, Photoelectrochemical cells. Nature **414**, 338–344 (2001)
2. X. Chen, S.S. Mao, Titanium dioxide nanomaterials: Synthesis, properties, modifications, and applications. Chem. Rev. **107**, 2891–2959 (2007)
3. S.P. Lim et al., Boosting photovoltaic performance of dye-sensitized solar cells using silver nanoparticle-decorated N,S-Co-DOped-TiO_2 photoanode. Sci. Rep. **5**, 11922 (2015)
4. R.A. Senthil et al., Enhanced performance of dye-sensitized solar cells based on organic dopant incorporated PVDF-HFP/PEO polymer blend electrolyte with g-C_3N_4/TiO_2 photoanode. J. Solid State Chem. **242**, 199–206 (2016)
5. J. Guo et al., One-step synthesis of mesoporous TiO_2 film for high photon-to-electron transport efficiency in dye-sensitized solar cells. J. Alloys Compd. **770**, 662–668 (2019)
6. L. Pan et al., Smart hybridization of TiO_2 nanorods and Fe_3O_4 nanoparticles with pristine graphene nanosheets: Hierarchically nanoengineered ternary heterostructures for high-rate lithium storage. Adv. Funct. Mater. **25**, 3341–3350 (2015)
7. L. Zheng et al., Hierarchical MoS_2 nanosheet@TiO_2 nanotube array composites with enhanced photocatalytic and photocurrent performances. Small **12**, 1527–1536 (2016)
8. Z. Yin, Graphene-based materials for solar cell applications. Adv. Energy Mater. **4**, 1300574 (2014)
9. J. Theerthagiri et al., Synthesis of various carbon incorporated flower-like MoS_2 microspheres as counter electrode for dye-sensitized solar cells. J. Solid State Electrochem. **21**, 581–590 (2017)
10. R.W. Mo et al., Facile synthesis of anatase TiO_2 quantum-dot/graphenenanosheet composites with enhanced electrochemical performance for lithium-ion batteries. Adv. Mater. **26**, 2084–2088 (2014)
11. F. Bonaccorso et al., Graphene, related two-dimensional crystals, and hybrid systems for energy conversion and storage. Science **347**, 1246501 (2015)
12. A.G. Shiravizadeh et al., Effects of annealing atmosphere and rGO concentration on the optical properties and enhanced photocatalytic performance of SnSe/rGO nanocomposites. PCCP **19**, 18089–18098 (2017)
13. R. Yousefi et al., The effect of defect emissions on enhancement photocatalytic performance of ZnSe QDs and ZnSe/rGO nanocomposites. Appl. Surf. Sci. **435**, 886–893 (2018)
14. M.A. Baghchesara et al., Improving the intrinsic properties of rGO sheets by S-doping and the effects of rGO improvements on the photocatalytic performance of Cu_3Se_2/rGO nanocomposites. Appl. Surf. Sci. **466**, 401–410 (2019)
15. S.P. Lim et al., In-situ electrochemically deposited polypyrrole nanoparticles incorporated reduced graphene oxide as an efficient counter electrode for platinum-free dye-sensitized solar cells. Sci. Rep. **4**, 5305 (2014)
16. B.L. Pang et al., Synthesis of $CoFe_2O_4$/graphene composite as a novel counter electrode for high performance dye-sensitized solar cells. Electrochim. Acta **297**, 70–76 (2019)
17. L.L. Zhang et al., Highly conductive and porous activated reduced graphene oxide films for high-power supercapacitors. Nano Lett. **12**, 1806–1812 (2012)

18. J.G. Radich et al., Is graphene a stable platform for photocatalysis? Mineralization of reduced graphene oxide with UV-irradiated TiO2 nanoparticles. Chem. Mater. **26**, 4662–4668 (2014)
19. A. Trapalis et al., TiO_2/graphene composite photocatalysts for NO_x removal: a comparison of surfactant-stabilized graphene and reduced graphene oxide. Appl. Catal. B **180**, 637–647 (2016)
20. C. Gomez-Navarro et al., Electronic transport properties of individual chemically reduced graphene oxide sheets. Nano Lett. **7**, 3499–3503 (2007)
21. G. Eda et al., Large-area ultrathin films of reduced graphene oxide as a transparent and flexible electronic material. Nat. Nanotechnol. **3**, 270–274 (2008)
22. P. Wang et al., Synthesis of reduced graphene oxide-anatase TiO_2 nanocomposite and its improved photo-induced charge transfer properties. Nanoscale **3**, 1640–1645 (2011)
23. J. Zhao et al., Improving the photovoltaic performance of dye-sensitized solar cell by graphene/titania photoanode. Electrochim. Acta **156**, 261–266 (2015)
24. Y. Liu et al., Formation and photovoltaic performance of few-layered graphene-decorated TiO_2 nanocrystals used in dye-sensitized solar cells. Nanoscale **6**, 6755–6762 (2014)
25. H. Zhang et al., One-step hydrothermal fabrication of TiO_2/reduced graphene oxide for high-efficiency dye-sensitized solar cells. J. Electron. Mater. **47**, 1630–1637 (2018)
26. D.T. Wang et al., Enhanced photoelectrocatalytic activity of reduced graphene oxide/TiO_2 composite films for dye degradation. Chem. Eng. J. **198**, 547–554 (2012)
27. M. Nawaz et al., One-step hydrothermal synthesis of porous 3D reduced graphene oxide/TiO_2 aerogel for carbamazepine photodegradation in aqueous solution. Appl. Catal. B **203**, 85–95 (2017)
28. D.B. Seong et al., A study of reduced graphene oxide/leaf-shaped TiO_2 nanofibers for enhanced photocatalytic performance via electrospinning. J. Solid State Chem. **266**, 196–204 (2018)
29. WS Hammers Jr, R.E. Offeman, Preparation of graphitic oxide. J. Am. Chem. Soc. **80**, 1339 (1958)
30. D.R. Dreyer et al., The chemistry of graphene oxide. Chem. Soc. Rev. **39**, 228–240 (2010)
31. J. Guo et al., One-step fabrication of TiO_2/graphene hybrid mesoporous film with enhanced photocatalytic activity and photovoltaic performance. Chin. J. Catal. **41**, 1208–1216 (2020)
32. B. Oregan, M. Gratzel, A low-cost, high-efficiency solar-cell based on dye-sensitized colloidal TiO_2 films. Nature **353**, 737–740 (1991)
33. L. Stobinski et al., Graphene oxide and reduced graphene oxide studied by the XRD, TEM and electron spectroscopy methods. J. Electron. Spectrosc. **195**, 145–154 (2014)
34. C. Xu et al., Synthesis of amphiphilic graphite oxide. Carbon **46**, 386–389 (2008)
35. P. Liu et al., Preparation and characterization of poly(vinyl acetate)-intercalated graphite oxide nanocomposite. J. Mater. Chem. **10**, 933–935 (2000)
36. F. Tian et al., Raman spectroscopy: a new approach to measure the percentage of anatase TiO_2 exposed (001) facets. J. Phys. Chem. C **116**, 7515–7519 (2012)
37. K.N. Kudin et al., Raman spectra of graphite oxide and functionalized graphene sheets. Nano Lett. **8**, 36–41 (2008)
38. J. Liu et al., Self-assembling TiO_2 nanorods on large graphene oxide sheets at a two-phase interface and their anti-recombination in photocatalytic applications. Adv. Funct. Mater. **20**, 4175–4181 (2010)
39. S.D. Perera et al., Hydrothermal synthesis of graphene-TiO_2 nanotube composites with enhanced photocatalytic activity. ACS Catal. **2**, 949–956 (2012)
40. G. Cheng et al., Novel preparation of anatase TiO_2@reduced graphene oxide hybrids for high-performance dye-sensitized solar cells. ACS Appl. Mater. Interfaces **5**, 6635–6642 (2013)
41. D. Lin et al., Layered reduced graphene oxide with nanoscale interlayer gaps as a stable host for lithium metal anodes. Nat. Nanotechnol. **11**, 626 (2016)
42. Y. Chen et al., FeS_2 nanoparticles embedded in reduced graphene oxide toward robust, high-performance electrocatalysts. Adv. Energy Mater. **7**, 1700482 (2017)
43. M.M. Byranvand et al., p-type CuI islands on TiO_2 electron transport layer for a highly efficient planar-perovskite solar cell with negligible hysteresis. Adv. Energy Mater. **8**, 1702235 (2018)
44. C. Zhang et al., Conformal carbon coated TiO_2 aerogel as superior anode for lithium-ion batteries. Chem. Eng. J. **351**, 825–831 (2018)
45. J. Chen et al., Unraveling the intrinsic structures that influence the transport of charges in TiO_2 electrodes. Adv. Energy Mater. **7**, 1700886 (2017)
46. F. Bonaccorso et al., Graphene photonics and optoelectronics. Nat. Photonics **4**, 611–622 (2010)
47. Y. Cao et al., Dye-sensitized solar cells with a high absorptivity ruthenium sensitizer featuring a 2-(hexylthio)thiophene conjugated bipyridine. J. Phys. Chem. C **113**, 6290–6297 (2009)
48. L.Y. Han et al., Modeling of an equivalent circuit for dye-sensitized solar cells. Appl. Phys. Lett. **84**, 2433–2435 (2004)
49. Y.-B. Tang et al., Incorporation of graphenes in nanostructured TiO_2 films via molecular grafting for dye-sensitized solar cell application. ACS Nano **4**, 3482–3488 (2010)
50. X. Huang et al., Hybrid nanostructures based on two-dimensional nanomaterials. Adv. Mater. **26**, 2185–2204 (2014)
51. B. Sun et al., Synthesis of mesoporous alpha-Fe_2O_3 nanostructures for highly sensitive gas sensors and high capacity anode materials in lithium ion batteries. J. Phys. Chem. C **114**, 18753–18761 (2010)
52. P.V. Kamat, Boosting the efficiency of quantum dot sensitized solar cells through modulation of interfacial charge transfer. Acc. Chem. Res. **45**, 1906–1915 (2012)
53. F. Raziq et al., Synthesis of large surface-area g-C_3N_4 comodified with MnO_x and Au-TiO_2 as efficient visible-light photocatalysts for fuel production. Adv. Energy Mater. **8**, 1701580 (2018)
54. J. Liang et al., MoS_2-based all-purpose fibrous electrode and self-powering energy fiber for efficient energy harvesting and storage. Adv. Energy Mater. **7**, 1601208 (2017)
55. K. Mahmood et al., 16.1% efficient hysteresis-free mesostructured perovskite solar cells based on synergistically improved ZnO nanorod arrays. Adv. Energy Mater. **5**, 1500568 (2015)